








High-sensitivity nanometamaterial near-infrared biosensor for label-free early cancer detection via exosomal biomarkers

MUSA N. HAMZA,¹  MOHAMMAD ALIBAKHSHIKENARI,^{2,3,*}  MOHAMMAD TARIQUL ISLAM,^{4,5}  SUNIL LAVADIYA,⁶ IFTIKHAR UD DIN,⁷ BRUNO SANCHES,⁸  SLAWOMIR KOZIEL,^{9,10} SYEDA IFFAT NAQVI,¹¹ MESSAOUD AHMED OUAMEUR,¹² ABINASH PANDA,¹³  ALI FARMANI,¹⁴  BAL VIRDEE,¹⁵ ZINELABIDDINE MEZACHE,¹⁶  AND MD. SHABIUL ISLAM^{17,18}

¹Department of Physics, College of Science, University of Raparin, Sulaymaniyah 46012, Iraq

²Lero, the Research Ireland Centre for Software, College of Science and Engineering, School of Computer Science, University of Galway, H91 TK33 Galway, Ireland

³Department of Electrical and Electronics Engineering, Dogus University, 34775 Umraniye, Istanbul, Türkiye

⁴Department of Electrical, Electronic and Systems Engineering, Faculty of Engineering and Built Environment, Universiti Kebangsaan Malaysia (UKM), 43600 Bangi, Selangor, Malaysia

⁵Computer and Information Sciences Research Center (CISRC), Imam Mohammad Ibn Saud Islamic University (IMSIU), Riyadh, Saudi Arabia

⁶Department of Information and Communication Technology, Marwadi University, Rajkot-360003 Gujarat, India

⁷Telecommunication Engineering Department, University of Engineering and Technology, Mardan 23200, Pakistan

⁸Department of Electronic Systems Engineering, Escola Politécnica da Universidade de São Paulo São Paulo, Brazil

⁹Engineering Optimization & Modeling Center, Reykjavik University, 102 Reykjavik, Iceland

¹⁰Faculty of Electronics, Telecommunications and Informatics, Gdansk University of Technology, 80-233 Gdansk, Poland

¹¹Department of Telecommunication Engineering, University of Engineering & Technology Taxila, Taxila, Pakistan

¹²Department of Electrical Engineering and Computer Engineering, University du Quebec a Trois-Rivières, Trois-Rivières, Quebec G9A 5H7, Canada

¹³Department of Electronics and Communication Engineering, CMR Institute of Technology, Bengaluru 560037, India

¹⁴Department of Electronics Engineering, Lorestan University, Khorramabad, Iran

¹⁵Center for Communications Technology, London Metropolitan University, SCDM, London N7 8DB, UK

¹⁶Institute of Optics and Precision Mechanics, University of Ferhat Abbas, Setif 1, Setif 19000, Algeria

¹⁷Centre for Advanced Devices and Systems, Centre of Excellence for Robotics and Sensing Technologies, Multimedia University (MMU), 63100 Cyberjaya, Selangor, Malaysia

¹⁸Faculty of Artificial Intelligence and Engineering, Multimedia University (MMU), 63100 Cyberjaya, Selangor, Malaysia

*mohammad.alibakhshikenari@universityofgalway.ie

Received 16 October 2025; revised 6 November 2025; accepted 6 November 2025; posted 7 November 2025; published 11 December 2025

This study presents a novel, to the best of our knowledge, ultra-wideband nanobiosensor based on a double-negative (DNG) metamaterial perfect absorber for early cancer detection through exosomal biomarker analysis. Our biosensor operates across a broad frequency range from 70 THz to 3 PHz, exhibiting near-unity absorption, i.e., exceeding 99%, and angular and polarization insensitivity, i.e., providing polarization-independent absorption across the full spectrum of polarization angles (0° to 90°), ensuring stable performance under both transverse electric (TE) and transverse magnetic (TM) polarized waves. Of particular interest is its performance in the near-infrared (NIR) region (70–400 THz), where the sensor's DNG characteristics manifest through simultaneously negative permittivity and permeability, enhancing field confinement and sensitivity. This spectral window is especially conducive to label-free, non-invasive detection of circulating exosomes, critical indicators of early stage oncogenesis. The sensor is constructed using a tri-layer metal–insulator–metal (MIM) architecture comprising nickel (Ni) layers and a silicon dioxide (SiO₂) dielectric spacer. The design leverages the plasmonic and thermal stability properties of Ni and the low optical attenuation of SiO₂ to achieve optimal absorption and structural robustness. Electromagnetic simulations demonstrate strong electric and magnetic resonances, producing significant near-field enhancements. These improve the detection of subtle dielectric changes associated with exosomal binding events. The sensor maintains high absorption efficiency across oblique incidence angles and various polarization states, making it suitable for real-world biomedical diagnostic applications. By focusing on the NIR regime where tissue transparency and molecular vibrational modes intersect, the proposed biosensor enables the discrimination between cancer-derived exosomes and their normal counterparts, as confirmed through spectral

and field distribution analyses. The demonstrated performance highlights the sensor's promise for next-generation photonic platforms targeting early cancer diagnostics, with potential extension to environmental monitoring and energy harvesting technologies.

Published by Optica Publishing Group under the terms of the [Creative Commons Attribution 4.0 License](#). Further distribution of this work must maintain attribution to the author(s) and the published article's title, journal citation, and DOI.

<https://doi.org/10.1364/AO.581804>

1. INTRODUCTION

In recent years, an emerging research field in absorbers is being established, the metamaterial (MTM)-based absorbers for the petahertz band [1].

This type of device can achieve almost perfect absorption in a large range of frequencies, while being extremely small, usually in the order of nanometers [2].

Metamaterials, distinguished by their exceptional capacity to manipulate electromagnetic waves in unconventional and highly controlled manners, have become a fundamental component of contemporary optical and electromagnetic engineering. The conceptual framework for these artificial media was established by Veselago in 1968 [3,4], who theoretically postulated the existence of materials with a negative refractive index, thereby initiating a paradigm shift in the understanding of light-matter interactions. This seminal insight laid the groundwork for the development of engineered structures capable of exhibiting negative permittivity (ϵ), negative permeability (μ), or simultaneous negativity in both parameters—phenomena seldom encountered in naturally occurring substances [5]. Such extraordinary electromagnetic responses enable precise control over propagation, reflection, and absorption processes, thereby facilitating novel device functionalities.

In recent years, metamaterials have garnered substantial attention across diverse scientific and technological disciplines, spanning biomedical engineering, photonics, and next-generation communication systems. Their integration has driven major advances in non-invasive diagnostics, biosensing, and high-resolution imaging, alongside the realization of compact, broadband, and energy-efficient components for modern wireless communication networks, multiple-input-multiple-output (MIMO) systems, millimeter-wave (mmWave) technologies, and super-wideband (SWB) antenna architectures. These developments extend across broad spectral regimes, encompassing gigahertz (GHz), terahertz (THz), near-infrared (NIR), and lower petahertz (PHz) frequencies [6–47].

Beyond these applications, metamaterials have also been employed extensively in telecommunications, optics, and sensing [48–72], as well as in emerging interdisciplinary technologies [2,5,73–75]. Their unique electromagnetic responses have enabled the realization of diverse devices such as super-lenses, cloaking structures, antennas, filters, and absorbers. Among these, metamaterial absorbers (MMAs) have garnered particular interest due to their efficient and broadband absorption capabilities, making them promising candidates

for applications in solar energy harvesting, thermal emission control, imaging, sensing, and photodetection [73].

The search for efficient broadband absorbers has led designers to explore novel MMA designs capable of achieving near-perfect absorption across wide frequency bands. One such design paradigm involves the utilization of a metal-insulator-metal (MIM) structure, where a dielectric spacer is sandwiched between metal layers to create adequate field interaction and enhance absorption efficiency [76]. Through meticulous material selection and precise geometric engineering, it is possible to optimize the absorption performance of MMAs while ensuring polarization insensitivity and acceptable angle stability [76,77].

Reviews on recent works have highlighted the significance of material properties in determining the performance of MMAs [78]. Systems utilizing gold in its MTMs may offer increased absorption rates due to the plasmonic effect, but their high cost necessitates alternatives. Some works used aluminum (Al), and it has proved to be a cost-effective substitute without compromising performance for THz and low PHz bands.

To enhance the development of ultra-broadband biosensing systems, we introduce a nano-engineered metamaterial biosensor exhibiting double-negative (DNG) characteristics, specifically tailored for the early stage detection of cancer through exosomal biomarkers. The proposed biosensor functions across an extensive spectral range spanning from 70 THz to 3 PHz, with a primary focus on the near-infrared (NIR) domain (70–400 THz), wherein both negative permittivity and permeability are distinctly manifested. Although DNG responses are sustained up to 500 THz, this study primarily concentrates on the 70–400 THz window due to its superior suitability for biosensing applications.

To realize broadband absorption characteristics, a tri-layer metal-insulator-metal (MIM) nanostructure was employed, comprising nickel (Ni) as both the resonator and ground layers, and silicon dioxide (SiO_2) as the dielectric interlayer. The Ni- SiO_2 -Ni assembly was chosen for its favorable thermal robustness, anti-corrosive behavior, and cost-efficiency, making it ideal for integration into biomedical diagnostic tools and solar thermophotovoltaic (STPV) platforms. Additionally, SiO_2 contributes to enhanced performance due to its low optical attenuation and excellent dielectric performance over a broad electromagnetic range, extending from the ultraviolet to the far-infrared.

Numerical simulations confirm the high-efficiency absorption performance of the designed double-negative nanometamaterial absorber (MMA), which demonstrates near-unity absorption levels. The device maintains insensitivity to

polarization and incidence angle, while effectively covering a broad spectral range from the far-infrared (FIR) to the ultraviolet (UV). This versatility facilitates its deployment in various optoelectronic fields, including biosensing, thermal imaging, energy conversion, and spectroscopic diagnostics.

A comparison with previously reported petahertz-band absorbers reveals the uniqueness of the present design. For instance, Mahmud *et al.* reported absorption exceeding 96% within 430–770 THz, reaching over 99% within a narrower spectral range [79]. Likewise, the study in [1] demonstrated a MIM-based absorber with an average absorption of 95%, peaking at 99.9% across the 187 THz–0.999 PHz visible band. Yang *et al.* developed a nanocone film absorber achieving over 98% mean absorption across 99.9 THz–0.999 PHz [80], while Lei *et al.* [81] utilized Al and Ti–Si cube configurations to realize 97% absorption from the visible to near-infrared region. Additionally, Bilal *et al.* presented a structure yielding 93% average absorption across 107 THz–0.749 PHz [82]. Despite these advancements, achieving stable DNG behavior across the FIR to EUV range remains a challenge, which this work addresses by extending the functionality into this underexplored spectral domain.

The NIR band (70–400 THz), positioned at the intersection of electronic and photonic technologies, is especially valuable for non-invasive biomedical imaging methods, including near-infrared spectroscopy and optical coherence tomography (OCT), which are pivotal for the early detection of cancer. Within this range, our DNG biosensor facilitates high-resolution, label-free identification of exosomes—key molecular messengers involved in oncogenesis, metastatic progression, immune modulation, and chemoresistance [83–86].

Traditional diagnostic modalities, such as MRI, CT, PET, and histopathology, often fall short in providing the sensitivity and specificity required for early stage cancer diagnosis [87–90]. Exosomes, a subclass of extracellular vesicles (EVs), offer a rich matrix of biomolecules—DNA, RNA, microRNA, and proteins—harvestable non-invasively from biological fluids like blood or urine [91]. These vesicles are increasingly recognized as highly reliable biomarkers in oncology.

In this framework, metamaterial-based perfect absorbers (MTMPAs) present a compelling platform for real-time, label-free exosome sensing in the NIR range [92–95]. Unlike conventional biochemical assays, such as ELISA that rely on molecular tagging, MTMPAs utilize plasmonic or resonant interactions at the nanoscale to detect physical binding events on the sensor's surface. This approach enables ultra-sensitive, real-time monitoring of exosomal dynamics and associated spectral shifts, thereby supporting the early detection of malignancies [96].

Beyond oncological diagnostics, the proposed MMA structure's adaptability extends to environmental applications, including the detection of chemical pollutants, and renewable energy harvesting systems. Its nanoscale architecture, coupled with DNG properties, allows for efficient electromagnetic energy capture, making it a valuable asset in spectroscopy and photonic devices.

This work introduces an ultra-wideband nanobiosensor employing a double-negative (DNG) metamaterial perfect absorber for early cancer detection via exosomal biomarkers.

Operating from 70 THz to 3 PHz, with emphasis on the near-infrared range, the sensor achieves near-unity absorption with angular and polarization insensitivity. A tri-layer Ni–SiO₂–Ni architecture ensures enhanced plasmonic resonance and structural stability. Electromagnetic simulations confirm strong near-field confinement and sensitivity to exosomal dielectric changes. The biosensor's performance enables non-invasive, label-free differentiation of cancerous from normal exosomes, underscoring its potential for next-generation biomedical diagnostics, as well as broader applications in photonics, environmental sensing, and energy harvesting.

2. MODEL'S UNIT CELL LAYOUT

Metamaterials possess inherent properties enabling effective absorption of electromagnetic radiation. Petahertz (PHz) waves interact with metamaterials, resulting in transmission, reflection, and absorption [Fig. 1(a)]. Perfect absorbers minimize reflection by absorbing most incident energy, while the metamaterial's architecture reduces destructive interference, enhancing absorption and attenuating transmitted waves. The absorber, constructed using a commercial full-wave finite integration approach (FIT) based on a high-frequency EM solver, facilitates analysis of metamaterials (MTMs) across various frequency ranges and boundaries. Scientists have employed numerical analysis to explore structures like perfect electric and magnetic conductors (PEC and PMC), unit cells, periodic arrays, and freespace.

Considerations of sensitivity, specificity, and selectivity are integral to the sensor's design, proposed for wavelengths spanning from the infrared (FIR) to the ultraviolet (EUV) spectrum [Fig. 1(b)]. Comprising three layers with dielectrics and full electrical conductors, the system's properties are summarized in Table 1. Large-scale integration, guided by computer-aided design (CST), allows verification of MTM properties and behavior across different frequencies and sizes. The model's three-layer design includes nickel (Ni) upper and lower layers and a silicon dioxide (SiO₂) dielectric pad. The nickel (Ni) layers are 4 nm thick, while the dielectric spacer is 15 nm thick, with nickel (Ni) exhibiting a conductivity of 1.44×10^7 S/m. The top nickel (Ni) layer is designed to match impedance with the incident medium, while the bottom nickel (Ni) layer, creating zero impedance, blocks incoming electromagnetic (EM) waves, essential for capturing and stopping wave propagation. Absorption parameters are obtained through electromagnetic (EM) waves interacting with the upper plane. Below are some

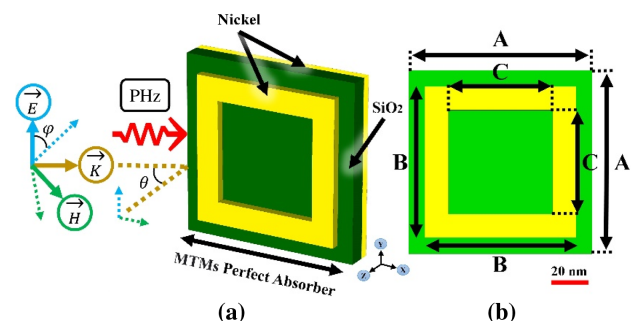


Fig. 1. Recommended structural design for a perfect absorber; (a) structural design and incident field directions of a perfect absorber and (b) Model 4 (proposed design).

Table 1. Complete List of the Variables That Have Been Adjusted for the Recommended Perfect MTM Absorber

Parameter	Value (nm)	Parameter	Value (nm)
A	100	SiO thick	15
B	82	Ni thick	4
C	56		

properties of nickel (Ni)— $13.1\text{e-}6\text{ K}^{-1}$, $1.44\text{e}+07\text{ S.m}^{-1}$, $91\text{ W.m}^{-1}\text{ K}^{-1}$, $0.45\text{ kJ.K}^{-1}.\text{kg}^{-1}$, $2.27216\text{e-}05\text{ m}^2.\text{s}^{-1}$, $0.31, 207\text{ kN.mm}^{-2}$, and 8900 kg.m^{-3} —which include thermal expansion, electrical conductivity (σ), thermal conductivity (k), specific heat capacity (Cs), diffusivity, Poisson's ratio, Young's modulus, and density, respectively.

To achieve accurate electromagnetic characterization of nanoscale double-negative (DNG) metamaterial absorbers operating in the petahertz (PHz) domain, particularly for biosensing applications in the near-infrared (NIR) regime, precise simulation protocols are essential. Utilizing CST Studio Suite, the simulation of perfect absorbers at the nanoscale requires careful attention to boundary condition configurations, meshing resolution, and wave excitation techniques.

A pivotal component in ensuring simulation fidelity is the implementation of perfectly matched layers (PMLs) at the simulation boundaries. These non-reflective boundary layers are essential for eliminating artificial back-reflections and for accurately modeling open-space conditions. In the context of PHz-frequency absorbers, the suppression of such reflections is critical to resolving fine absorption features and preserving energy confinement within the simulation domain.

The domain size in simulations must significantly exceed the physical dimensions of the metamaterial unit cell to reduce near-field boundary effects. Furthermore, adaptive and localized fine meshing—particularly around metallic nanostructures and sharp edges—is required to capture the high spatial gradients of the electric and magnetic fields intrinsic to metamaterial resonances.

Accurate wave excitation is another crucial parameter. In this study, plane wave sources are predominantly utilized, necessitating precise control over polarization direction and wave vector alignment to ensure uniform field distribution across the metamaterial surface. In specific cases where modal propagation is analyzed, waveguide port excitations may also be employed to evaluate the interaction of guided waves with the absorber structure.

The material parameters of the nano-engineered absorber—especially for metals like nickel (Ni) and substrates such as silicon dioxide (SiO_2)—must be rigorously defined based on their complex frequency-dependent permittivity and permeability in the NIR regime. Exploiting symmetry planes and boundary conditions further enhances computational efficiency while preserving accuracy.

Post-processing tools in CST Studio allow for the extraction of critical performance metrics such as absorptance, reflection coefficients, and field enhancement profiles. These metrics are essential in evaluating the biosensor's performance and its capability to detect exosomal biomarkers by identifying localized field enhancements and absorption peaks associated with biomolecular interactions.

As shown in Fig. 1, the proposed design, Model 4, demonstrates an optimized geometric configuration tailored to maximize absorption in the NIR spectrum. The structural blueprint combines subwavelength periodicity and double-negative effective parameters to support strong electric and magnetic resonances, essential for high sensitivity and selectivity in exosome detection.

The strategic integration of PMLs, broadband plane wave excitation, and precise meshing schemes enables robust simulation of the metamaterial's electromagnetic behavior across the PHz frequency range. This forms the foundational basis for the development of ultra-compact, label-free biosensors with superior field confinement, making them ideal for the early stage detection of cancer through exosomal biomarker analysis.

3. RESULTS AND ANALYSIS

This section delves into the detailed findings and analysis of the proposed metamaterial-based absorber design. Organized into four subsections, the results offer a comprehensive examination of various absorption properties, spectral characteristics, material parameters, and field distributions represented by Figs. 2–13.

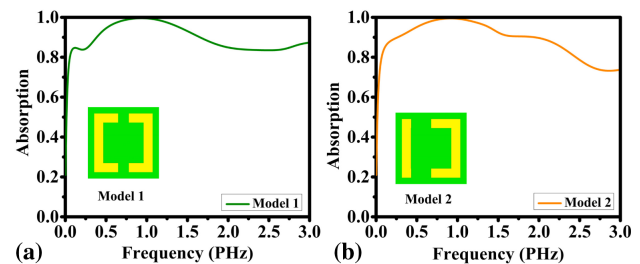


Fig. 2. These are the different absorption properties of the two designs: (a) Model 1 and (b) Model 2.

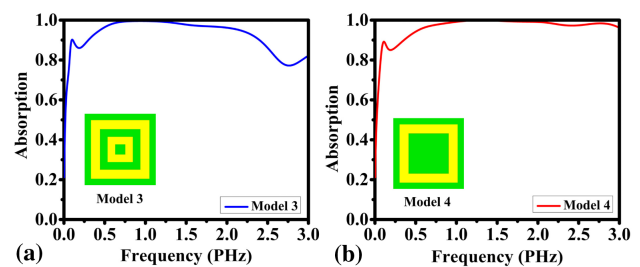


Fig. 3. These are the various absorption qualities of the two designs: (a) Model 3 and (b) Model 4.

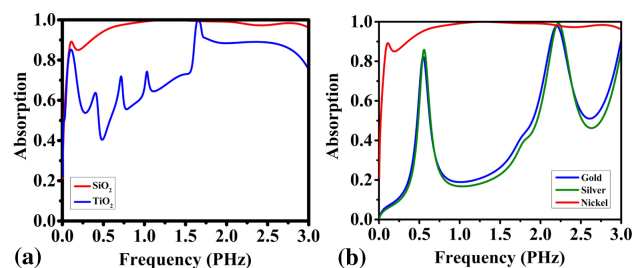


Fig. 4. Absorption spectra for the suggested design under various: (a) substrate material and (b) resonator material conditions.

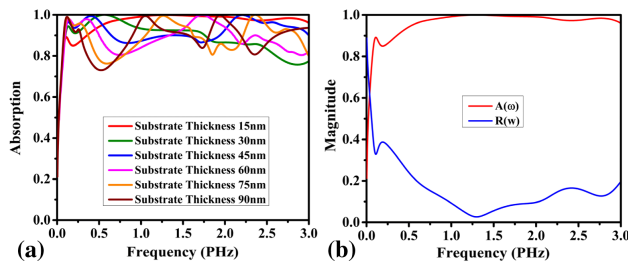


Fig. 5. (a) Investigating the effect of the proposed substrate thickness on the ability to absorb and (b) the reflection spectrum and absorption spectrum of the absorber.

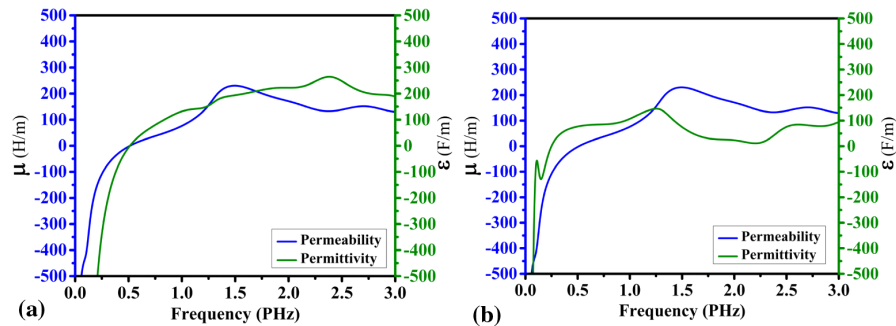


Fig. 6. (a) Real parts of permeability μ and permittivity ϵ and (b) imaginary parts of permeability μ and permittivity ϵ of the proposed absorber.

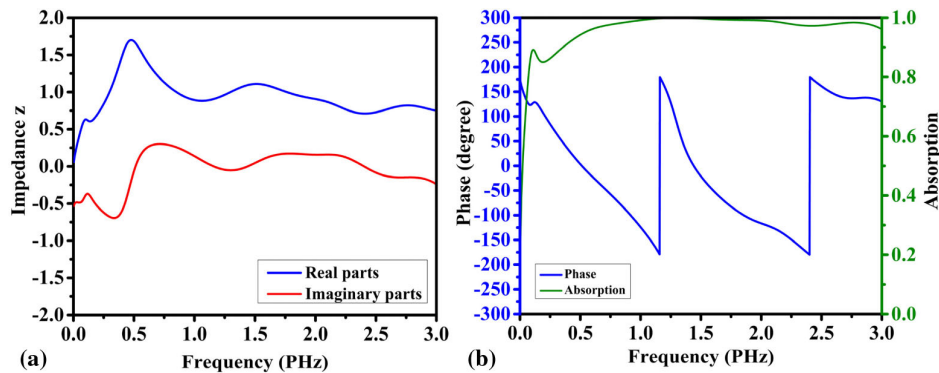


Fig. 7. Simulated responses of parameters of the proposed model. (a) Impedance z and (b) phase.

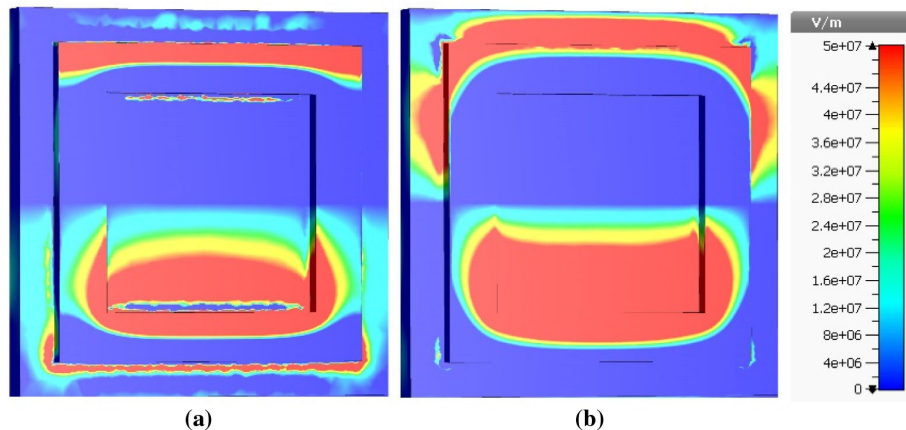


Fig. 8. Distributions of the metamaterial structure field are shown on a color map: (a) E_z -field real parts and (b) E_z -field imaginary part.

A. Absorption Response of the Proposed Models

The absorption performance of the proposed nanometamaterial biosensor structures, designed to operate in the near-infrared (NIR) petahertz regime, is systematically evaluated across four distinct models—each demonstrating ultra-wideband absorption characteristics with high efficiency across a broad spectral range.

In Fig. 2(a), Model-1 displays a strong absorption profile, achieving a peak absorbance of 99.99% near 0.95 PHz, while maintaining absorption levels around or above 90% throughout the 0.5–2.5 PHz range. The observed absorption spectrum is not limited to a single sharp resonance but rather exhibits a wavy

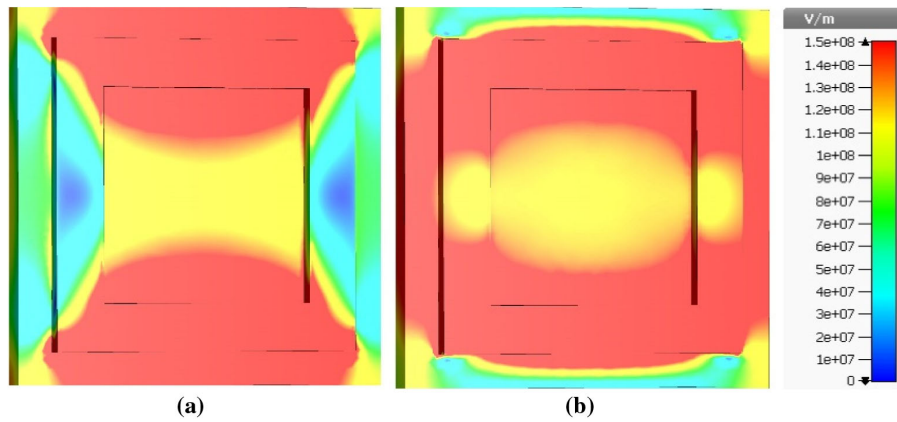


Fig. 9. Distributions of the metamaterial structure field are shown on a color map: (a) /E/-field real parts and (b) /E/-field imaginary part.

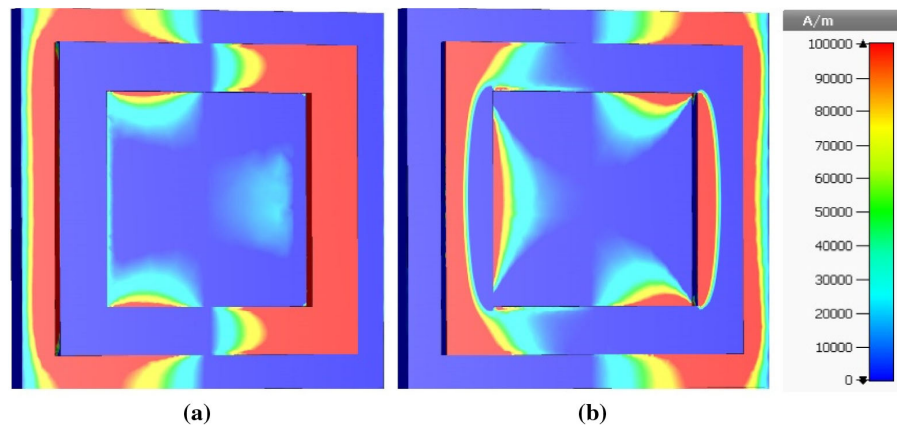


Fig. 10. Distributions of the metamaterial structure field are shown on a color map: (a) Hz-field real parts and (b) Hz-field imaginary part.

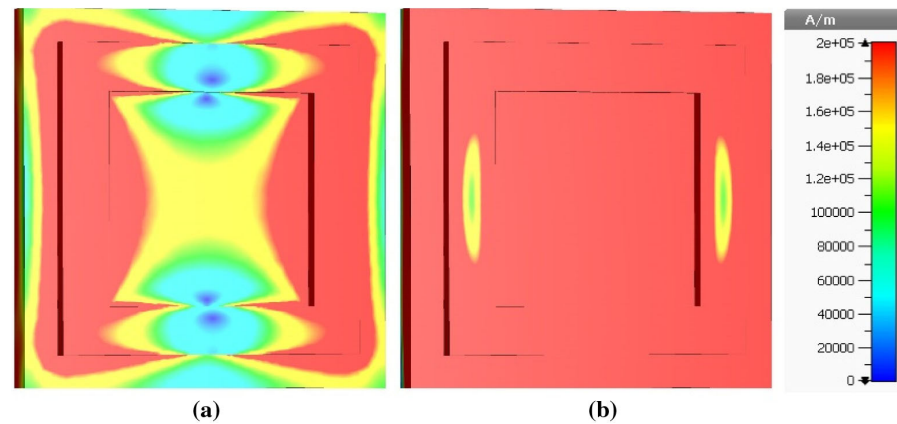


Fig. 11. Distributions of the metamaterial structure field are shown on a color map: (a) /H/-field real parts and (b) /H/-field imaginary part.

broadband profile, indicative of multiresonant behavior and efficient coupling across a wide frequency domain.

Model-2, shown in Fig. 2(b), demonstrates similarly robust ultra-wideband characteristics, sustaining over 90% absorption from 0.5 to 2 PHz, with a maximum absorptance of 99.98% at approximately 1 PHz. The slight geometric modifications in this model result in improved impedance matching and enhanced field confinement, contributing to its stable and distributed absorption performance across the operating band.

In Fig. 3(a), the absorption behavior of Model-3, incorporating dual O-shaped resonators with deliberate structural deformations, exhibits further enhancement in performance. This model shows over 99% absorption across a broad region from 0.7 to 1.5 PHz, while preserving a high average absorption rate across an even wider band, attributed to improved resonant current distribution and electromagnetic energy trapping within the structure.

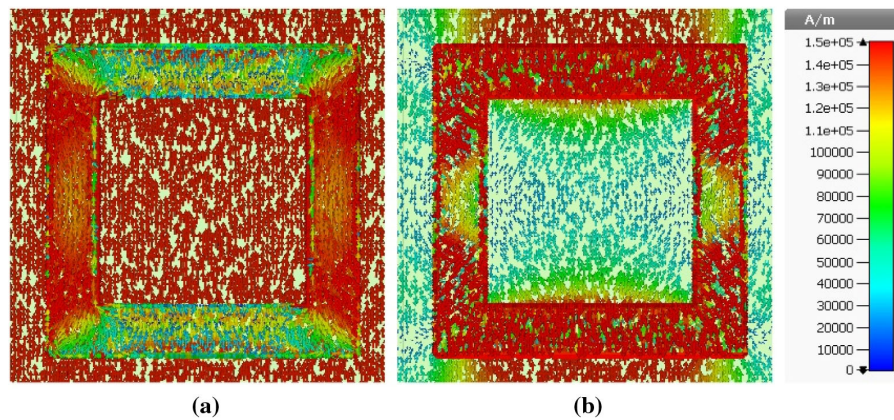


Fig. 12. Surface current distribution of the recommended metamaterial: (a) real part and (b) imaginary part.

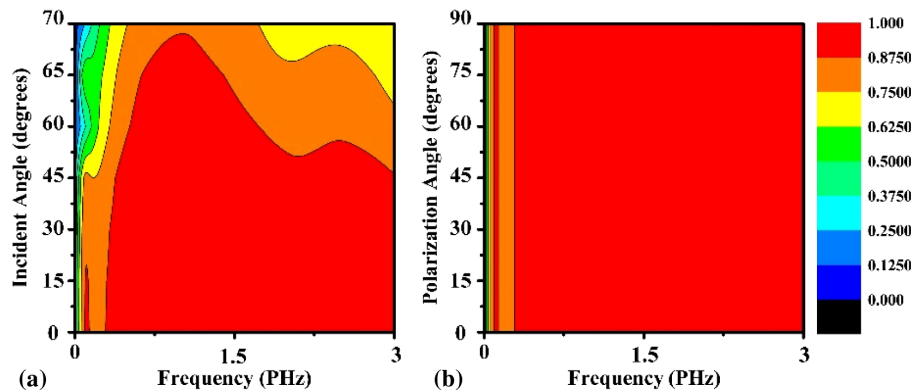


Fig. 13. Impact of angle modification on absorption rate is investigated for (a) incidence angle and (b) polarization angle.

Model-4, depicted in Fig. 3(b), represents the most optimized configuration. It delivers absorption consistently above 90% across an extended bandwidth from 0.5 to 3 PHz. The design promotes effective excitation of surface modes and exhibits multimodal resonance behavior, enabling efficient absorption over the entire spectral span. The wavy nature of the absorption curve, with localized peaks and troughs, highlights the underlying multiresonant mechanisms without compromising ultra-wideband performance.

Collectively, the comparative analysis of all four models emphasizes the critical role of geometric tailoring in optimizing ultra-broadband and high-efficiency absorption. The results confirm that each model—despite slight variations in peak absorptance—operates effectively over a broad Petahertz-range spectrum. Such broadband characteristics are particularly advantageous for biosensing applications where diverse exosomal biomarkers may exhibit variable spectral responses. This reinforces the proposed biosensor's applicability in non-invasive, real-time early cancer detection in the near-infrared regime.

B. Effect of Substrate Materials and Thickness

The analysis for varying substrate material is shown in Fig. 4(a). There are two different materials SiO_2 and TiO_2 considered for the absorption response observation. The incorporation of SiO_2

substrate material represents a good absorption response over the wide spectrum compared to the TiO_2 substrate.

The analysis for different resonating materials is considered and analyzed for the absorption response. Gold, silver, and nickel materials are taken into consideration for the analysis. More confine and best absorption response is observed in the nickel resonating material. The gold and silver as resonating materials respond to three absorption peaks. The overall response of gold and silver is poor compared to nickel as shown in Fig. 4(b).

The substrate material thickness variation is shown in Fig. 5(a). The thickness variation is taken over 15–90 nm with a step size of 15 nm. The peak absorption response is observed for 15 nm. Other variations have lower absorption compared to 15 nm substrate thickness. The absorption and reflectance responses are opposite to each other as shown in Fig. 5(b). The minimum reflectance response of suggested structure is observed at 1.25 PHz.

C. Electromagnetic Properties and Impedance Behavior of the Proposed Sensor

To evaluate the underlying electromagnetic characteristics of the proposed nanometamaterial biosensor, a detailed analysis of its effective permittivity (ϵ) and permeability (μ) was conducted. As illustrated in Fig. 6(a), the real components of ϵ and μ reveal a distinct double-negative (DNG) behavior within the spectral

window of 70–400 THz, corresponding to the near-infrared (NIR) regime. This region is of particular interest for biosensing applications due to its ability to penetrate biological tissues non-invasively and its sensitivity to molecular vibrational and rotational modes.

The imaginary parts of ϵ and μ , presented in Fig. 6(b), further support the existence of resonant metamaterial features, indicative of energy dissipation and field confinement within the sensor structure. The simultaneous negativity of both ϵ and μ enables exotic electromagnetic phenomena, such as negative refraction and reversed phase velocity, which contribute to the sensor's enhanced electromagnetic confinement and absorption performance.

This DNG behavior is instrumental in achieving efficient and broadband absorption over the target frequency range, enhancing the sensor's capability to detect weak electromagnetic signals associated with biomolecular interactions. Specifically, the ability to isolate and amplify the spectral signatures of exosomes—membrane-bound extracellular vesicles carrying nucleic acids, proteins, and lipids—positions this sensor as a powerful platform for early stage cancer detection.

The impedance characteristics of the sensor, shown in Fig. 7(a), provide further insight into its energy transfer efficiency and resonant behavior. The real part of the impedance corresponds to resistive losses, while the imaginary part reflects the reactive (capacitive or inductive) nature of the structure. Optimized impedance matching, indicated by a normalized impedance close to unity, ensures minimal reflection and maximal absorption of incident electromagnetic waves. This is a crucial feature for biosensors intended to function across a broad frequency spectrum, where impedance mismatches typically result in reduced sensitivity and signal degradation.

In addition, the phase response illustrated in Fig. 7(b) exhibits distinct variations at key frequencies around 1.2 and 2.45 PHz, indicating strong resonance behavior and spectral phase transitions that are highly sensitive to the local dielectric environment. Such phase shifts can be leveraged for real-time monitoring of analyte binding events at the sensor surface, offering a dynamic and label-free approach to biomolecular detection.

Collectively, the observed DNG electromagnetic response and impedance-phase characteristics underscore the advanced functional capabilities of the proposed biosensor. These features not only enable high absorption efficiency and spectral selectivity in the NIR range but also support its broader applicability across the terahertz to petahertz regime, positioning the sensor as a promising tool for ultra-sensitive, non-invasive exosomal biomarker detection in early cancer diagnostics.

D. Metamaterial Structure Field Distributions and Parameter Responses

To further elucidate the functional behavior of the proposed nanometamaterial-based biosensor, comprehensive electromagnetic field distribution analyses were conducted using CST Microwave Studio. These simulations focused on the electric field component along the z axis (E_z -field) and the overall magnitude of the electric field ($|E|$ -field), both of which are critical to understanding the sensor's absorption mechanisms and energy

confinement capabilities in the near-infrared (NIR) to petahertz (PHz) spectral regime.

Figures 8(a) and 8(b) illustrate the real and imaginary parts of the E_z -field distribution, respectively. These components reveal spatial variations of the vertical electric field across the metamaterial surface. The real part of the E_z -field corresponds to the in-phase component of the electric field, highlighting regions of energy storage and directionality along the z axis. In contrast, the imaginary part reflects the out-of-phase component, providing insight into energy dissipation due to intrinsic material losses such as resistivity and surface currents within the nanostructured resonators.

The distribution maps exhibit a predominantly blue coloration throughout most of the sensor surface, indicating relatively uniform and stable field intensities and phase behavior across the active sensing region. However, the presence of red hotspots at the upper and lower boundaries of the structure signifies zones of intensified electromagnetic activity and notable phase fluctuation. These localized field enhancements play a vital role in augmenting the biosensor's sensitivity, particularly in its interaction with weak electromagnetic signals emanating from biological nanostructures such as exosomal biomarkers.

Complementing the E_z -field analysis, Figs. 9(a) and 9(b) depict the spatial distributions of the real and imaginary parts of the $|E|$ -field (i.e., the magnitude of the electric field irrespective of orientation). The real part captures the amplitude and vector orientation of the electric field, while the imaginary component provides phase-related information and energy dissipation characteristics. These visualizations are instrumental in identifying areas of strong field localization, which are directly correlated with the sensor's absorption efficiency and biomolecular interaction potential.

The color distribution in these maps highlights critical electromagnetic behaviors within the metamaterial architecture. The prevalence of red in the central and boundary regions indicates high field intensity and significant phase modulation, whereas the blue gradients toward the periphery suggest weaker electromagnetic interactions. The observed yellow bands in the center point to a transitional electromagnetic activity zone, indicative of energy transfer and localized resonant behavior. Such spatial field inhomogeneity underscores the effectiveness of the metamaterial layout in concentrating electromagnetic energy, thereby enhancing its biosensing capabilities.

The sensor design incorporates a periodic array of nickel (Ni) nanostructures (100 nm \times 100 nm with 4 nm thickness) mounted on a 100 nm thick silicon dioxide (SiO_2) substrate. This configuration facilitates the emergence of strong field confinement within subwavelength volumes, especially in the NIR region (70–400 THz). These localized fields dramatically boost the electromagnetic interaction with exosomes, enabling detection of their distinct spectral signatures with high fidelity. This mechanism is pivotal in the early stage diagnosis of cancer, as exosomes are known to carry a rich cargo of oncogenic proteins and nucleic acids.

Moreover, the field enhancement enabled by the sensor's double-negative (DNG) characteristics—arising from simultaneously negative permittivity (ϵ) and permeability (μ)—leads to exceptional confinement and absorption of incident radiation. This makes the structure highly responsive to minuscule

dielectric perturbations induced by trace concentrations of exosomal biomarkers, thus positioning the proposed biosensor as a promising candidate for label-free, non-invasive, and highly sensitive early cancer diagnostics.

Analyzing the Hz-field in CST Studio offers crucial insights into their electromagnetic behavior. The real part of the Hz-field portrays the storage or in-phase component of the magnetic field along the z axis. It illustrates the amount of magnetic energy stored within the sensor's structure at different spatial points and temporal instances. Positive values denote magnetic field orientations pointing upward along the z axis at specific locations and times, while negative values indicate downward field orientations. Conversely, the imaginary part of the Hz-field signifies the dissipative or out-of-phase component of the magnetic field along the z axis. This aspect relates to energy loss within the metamaterial due to properties such as conductivity and resistance. Positive imaginary values signify energy absorption from incident waves by the sensor, whereas negative values suggest energy release back into the electromagnetic field. Understanding both the real and imaginary components of the Hz-field enables a comprehensive analysis of the sensor's performance. This comprehension aids in optimizing the sensor's design to enhance its absorption capabilities across the infrared to ultraviolet spectrum, providing diverse applications in sensing and detection. In Fig. 10, the distribution of the field within a metamaterial structure is illustrated using a color map. Figure 10(a) shows the real components of the Hz-field, where areas with minimal energy absorption or transmission loss are displayed in a uniform blue color. However, the presence of red color at the boundaries implies differences in absorption or transmission properties, likely due to interactions with adjacent boundaries. These regions demonstrate heightened absorption or transmission capabilities, indicating localized effects such as resonances or scattering phenomena. In Fig. 10(b), the imaginary part of the Hz-field is represented mainly by a consistent blue color, indicating minimal absorption or loss. Similar to Fig. 10(a), the appearance of red color at the boundaries signifies deviations in absorption or transmission behaviors. These variations are influenced by unique material characteristics or geometric attributes, affecting the absorption and transmission of electromagnetic waves within the metamaterial structure.

The absolute value of the magnetic field ($|H|$ -field) is essential for analyzing electromagnetic interactions in metamaterial-perfect absorber sensors. While the electric field primarily governs light absorption, the magnetic field significantly influences electromagnetic wave propagation and polarization. In CST Studio, the real part of the $|H|$ -field indicates the magnitude and direction of the magnetic field, while the imaginary part signifies energy dissipation or phase shifts. Analyzing both parts provides insights into the spatial distribution, strength, and absorption efficiency of the magnetic field within the sensor design across the FIR to EUV spectrum. This understanding facilitates optimization for enhanced electromagnetic wave manipulation and absorption, contributing to the sensor's performance and versatility in various applications. The diagram presented in Fig. 11 illustrates the spatial distributions of the field in a metamaterial structure using a color map visual representation. In Fig. 11(a), the colors red, blue, and yellow represent the real parts of the H-field, indicating varying

field intensities. The yellow color in the central area suggests a higher concentration of the field, potentially implying enhanced absorption properties in that specific region. On the contrary, the blue and yellow color distributions on the sides imply lower field concentration or absorption properties compared to the central region. Moving on to Fig. 11(b), which displays the imaginary part of the H-field, the entire field is uniformly colored red. This consistent red color suggests a steady level of absorption across the structure, indicating uniform energy absorption across the full frequency spectrum. Such absorption characteristics could lead to modifications in the structure's properties, affecting its overall performance in applications like frequency filtering or signal manipulation.

Figure 12 displays the distribution of surface currents in a recommended metamaterial designed for absorber applications. In the first Fig. 12(a), the dominant flow of current is shown in a consistent red color, with variations in current density indicated by a blue–yellow combination at the top and bottom portions of the patch. This distribution is vital for effectively absorbing electromagnetic waves over various frequencies. On the other hand, Fig. 12(b) presents the imaginary part, characterized by a uniform blue–yellow combination, signifying the reactive component of the surface current. Interestingly, the patch appears completely red, denoting a concentrated current flow, particularly on the top and bottom sides. This unique distribution pattern is made to amplify the absorptive qualities of the metamaterial. By controlling the surface current in this way, the metamaterial can efficiently attenuate incident electromagnetic waves, making it suitable for a range of applications such as stealth technology, sensing, and energy harvesting.

The angular response of the proposed nanometamaterial-based double-negative (DNG) biosensor was systematically evaluated to assess its robustness and reliability under varying illumination conditions, as presented in Fig. 13. This investigation is critical for biosensing applications in the near-infrared (NIR) regime, where incident light may interact with the sensor at oblique or variably polarized angles, particularly when integrated into real-world diagnostic platforms.

In Fig. 13(a), the sensor's absorption behavior was analyzed across a wide range of incidence angles from normal incidence up to 70° , simulating conditions in which exosomal biomarkers may be illuminated from varying directions. The simulation results demonstrate that the proposed DNG biosensor maintains high and stable absorbance levels, exhibiting negligible performance degradation up to large oblique angles. This angular insensitivity is a direct result of the carefully engineered structural symmetry and the strong magnetic and electric resonances sustained within the subwavelength unit cells of the metamaterial absorber. Such stability under angular variation is essential for ensuring accurate and reliable biosensing performance, independent of the directional alignment of incoming radiation.

Figure 13(b) further investigates the sensor's resilience to variations in polarization angle, assessing how changes in the electric field vector orientation of the incident wave influence absorption. The biosensor exhibits near-polarization-independent absorption behavior across the full range of polarization angles (0° – 90°), confirming its ability to function effectively under both transverse electric (TE) and transverse magnetic (TM)

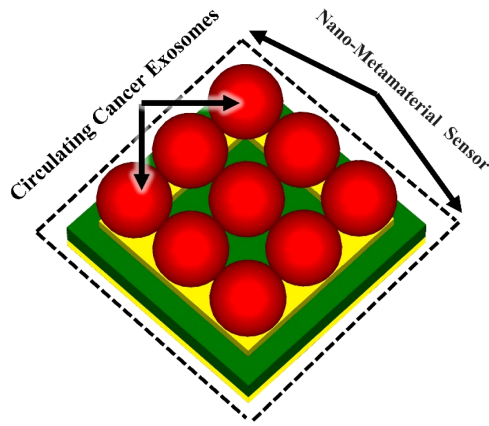


Fig. 14. Schematic representation of the nanometamaterial-based biosensor, illustrating the spatial distribution and interaction dynamics of electric and magnetic fields in the presence of both healthy and malignant circulating exosomes.

polarized waves. This polarization insensitivity arises from the isotropic surface current distributions and dual-resonant features inherent to the double-negative design, which collectively contribute to uniform electromagnetic field confinement and resonance excitation regardless of polarization orientation.

The visual representation in Fig. 13 illustrates these findings through a color-coded mapping of absorption intensity, where transitions from red to brown, yellow, and a combination of blue and green [in Fig. 13(a)] represent the angular evolution of the incident wave, and corresponding resonance shifts. In Fig. 13(b), the emphasized red and brown zones in the left corner reflect the sensor's steady absorption at varying polarization orientations, indicating minimal fluctuation in absorption efficiency.

The demonstrated angle and polarization robustness of the biosensor underscores its versatility in diverse diagnostic environments, where the alignment of incident light cannot always be controlled. This feature enhances its potential for practical implementation in non-invasive optical detection platforms, enabling consistent detection of exosomal biomarkers irrespective of the light source orientation. Thus, the angle-resilient design of the proposed DNG metamaterial biosensor contributes significantly to the development of next-generation, high-performance diagnostic tools for early stage cancer detection.

4. CHARACTERIZATION AND DIFFERENTIATION OF CIRCULATING EXOSOMES FOR CANCER DETECTION

The identification and differentiation of circulating exosomes are vital for the early diagnosis of cancer, offering a non-invasive alternative to conventional histopathological and imaging techniques. Exosomes, nanoscale, extracellular vesicles secreted by both normal and malignant cells carry a molecular cargo comprising proteins, RNA, and lipids reflective of their cellular origin. This cargo, along with their size, density, and membrane composition, makes exosomes highly suitable as biomarkers for early stage cancer detection.

The proposed nanometamaterial biosensor, leveraging double-negative (DNG) properties within the ultra-wideband spectrum of 70 THz to 3 PHz, is engineered to detect subtle dielectric variations caused by exosomal binding. As shown in Fig. 14, the sensor supports strong field localization and interaction dynamics across the full 0–3 PHz frequency range, which is critical for capturing the unique spectral signatures of different exosome populations. This broad operational bandwidth enables comprehensive characterization of both normal and cancer-derived exosomes across multiple photonic and near-infrared sub-bands.

The sensor's enhanced field confinement, stemming from its DNG metamaterial design, amplifies electromagnetic interactions at the nanoscale. These effects are captured in the sensor's reflection coefficients (S_{11}), with distinct shifts in both real and imaginary components depending on the type of exosome present, as illustrated in Fig. 15.

Cancerous exosomes, due to their altered membrane composition and higher refractive index, produce stronger spectral shifts and resonance perturbations than normal exosomes.

The near-infrared microwave imaging (MWI) results presented in Figs. 16 and 17 offer compelling evidence of the proposed nanometamaterial biosensor's capacity for selective exosomal detection based on their electromagnetic field interactions. Specifically, Fig. 16 illustrates the electric field (E-field) distribution at 100 THz, where a marked enhancement in field intensity and spatial confinement is observed in the presence of malignant exosomes. This behavior can be attributed to the increased molecular density and altered dielectric properties of cancer-derived exosomes, which result in elevated local permittivity and stronger polarization under incident electromagnetic radiation. These localized dielectric discontinuities at the nanoscale enhance the electromagnetic field concentration through plasmonic and dielectric resonance effects, thereby amplifying the E-field distribution within the metamaterial sensor surface.

Complementing the electric field analysis, Fig. 17 provides the MWI depiction of the magnetic field (H-field) distribution at 400 THz. The biosensor exhibits more pronounced magnetic field localization when interacting with malignant exosomes, as evidenced by the field intensity reaching up to 3.5×10^5 A/m [Fig. 17(b)], in contrast to 3.0×10^5 A/m for normal exosomes [Fig. 17(a)]. These results underscore the dual-mode sensitivity of the biosensor to both electric and magnetic field perturbations, a hallmark of its double-negative (DNG) metamaterial characteristics.

This dual-field sensitivity enables broadband, label-free discrimination of exosomal biomarkers, facilitating high-resolution detection across the full operational frequency spectrum (70 THz to 3 PHz). The strong near-field enhancements generated at specific resonance frequencies allow the sensor to detect minute dielectric variations due to biomolecular binding, even in low-concentration or heterogeneous exosome populations. Moreover, the ability to differentiate exosomal origin based on nanoscale E-field and H-field mapping highlights the biosensor's potential in real-time, non-invasive diagnostics.

The underlying resonant phenomena, driven by the interaction of incident PHz waves with the engineered

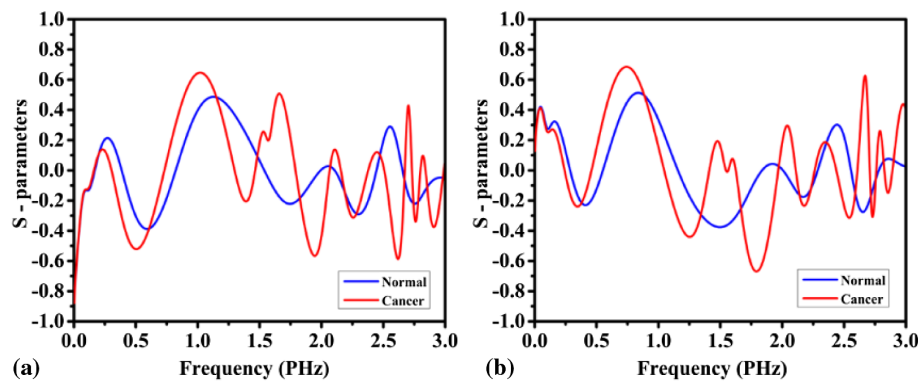


Fig. 15. Spectral analysis of the nano-engineered biosensor's response for discriminating between normal and cancer-associated exosomes over a broad frequency range (70 THz–3 PHz): (a) real part of the reflection coefficient (S_{11}) and (b) imaginary part of the reflection coefficient (S_{11}).

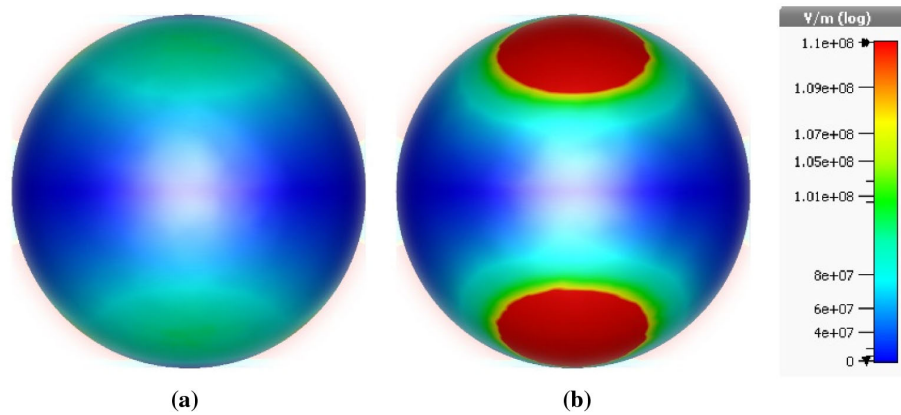


Fig. 16. Near-infrared-based microwave imaging (MWI) results depicting the electric field (E-field) distribution at 100 THz for exosomal analysis: (a) distribution pattern for normal exosomes and (b) distribution pattern for malignant exosomes.

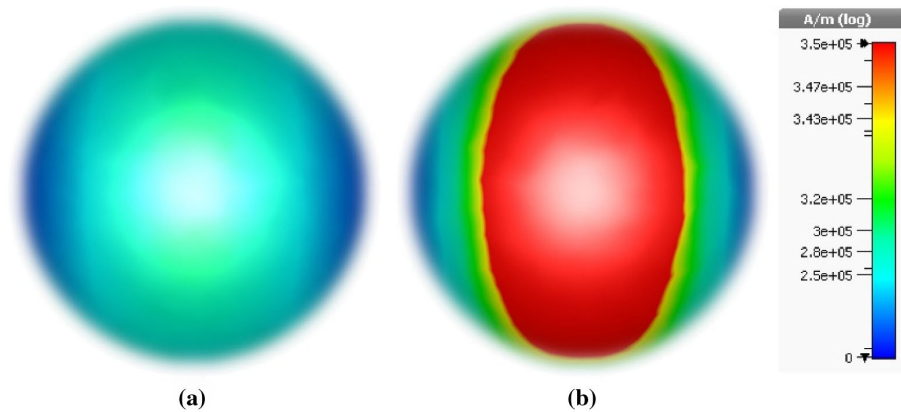


Fig. 17. Visualization of the magnetic field (H-field) distribution captured at 400 THz using the proposed biosensor configuration: (a) magnetic field interaction with normal exosomes and (b) magnetic field interaction with cancer-derived exosomes.

nanometamaterial structure, produce field enhancements critical to optimizing sensor performance. The Ni–SiO₂–Ni tri-layer design not only supports efficient plasmonic excitation but also offers thermal and chemical stability essential for biological interfacing. These field distributions reveal the biosensor's capacity to achieve maximal absorption and field confinement, thus validating its design for sensitive cancer exosome detection.

Together, these E-field and H-field profiles offer a comprehensive view of the resonance behavior and field–matter

interactions within the nanometamaterial structure. The strong contrast in field intensities between malignant and normal exosomes confirms the biosensor's capability for precise discrimination and underlines its utility in early cancer diagnostics. The integration of ultra-wideband spectral analysis with sub-wavelength field confinement affirms the proposed system as a promising diagnostic tool, with potential applicability to a broad spectrum of diseases involving exosomal biomarkers.

Table 2. Comparative Analysis with Relevant Work

Reference	Material	Unit Cell Dimension (nm)	Operation Range (PHz)	Bandwidth (PHz)	Angular Stability	Absorption
[97]	Ni, SiO ₂	200 × 200 × 96	0.1–1.39	1.29	80% absorption for $\theta \leq 60$	95.91%
[1]	Ni, SiO ₂	300 × 300 × 170	0.18–0.99	0.81	70% absorption for $\theta \leq 70$	>91.27%
[82]	Ni, SiO ₂	200 × 200 × 125	0.11–0.75	0.64	80% absorption for $\theta \leq 60$	93%
[98]	W, SiO ₂	200 × 200 × 242	0.12–0.75	0.63	80% absorption for $\theta \leq 45$	92%
[99]	W, Al ₂ O ₃ , Ti	1000 × 1000 × 320	0.16–0.6	0.44	94% absorption for $\theta \leq 60$	94%
[100]	Ni, AlN	75 × 75 × 50	0.1–0.75	0.65	70% absorption for $\theta \leq 60$	90%
[101]	Ti, SiO ₂ , Si ₃ N ₄	750 × 750 × 550	0.10–0.36	0.26	85% absorption for $\theta \leq 60$	95%
[102]	Cr, SiO ₂	160 × 160 × 85	0.39–0.75	0.36	80% absorption for $\theta \leq 60$	96%
Proposed	Ni, SiO ₂	100 × 100 × 23	0.07–3	2.93	80% absorption for $\theta \leq 70$	>95%

5. BENCHMARKING

The proposed design introduces a broadband metamaterial absorber (MTMA) that operates effectively across an ultra-wide frequency range extending from the mid-infrared (MIR) to the ultraviolet (UV) spectrum. The sensor exhibits several outstanding features, including compactness, high absorption efficiency, notable sensitivity, angular stability, and polarization insensitivity. As demonstrated in Table 2, the proposed absorber surpasses many recently reported designs in these performance metrics.

The sensor operates over an ultra-wide frequency range spanning from 70 THz to 3 PHz, achieving an exceptional average absorption rate exceeding 99%. Critically, the structure employs double-negative metamaterial properties—exhibiting both negative permittivity and negative permeability—within the near-infrared region (70–500 THz), thereby significantly enhancing sensitivity for early cancer detection through exosome-based analysis. Furthermore, the sensor demonstrates functional versatility across diverse spectral domains, facilitating applications in biomedical engineering, energy harvesting, and molecular diagnostics.

Particularly, the sensor is optimized to operate within the 70–400 THz range, with all geometric parameters carefully designed to support non-invasive imaging modalities such as optical coherence tomography (OCT) and near-infrared (NIR) spectroscopy—both of which are critical tools for early stage cancer detection.

Another key characteristic of the proposed biosensor is its polarization-independent absorption across the full spectrum of polarization angles (0°–90°), ensuring stable performance under both transverse electric (TE) and transverse magnetic (TM) polarized waves. Additionally, the sensor is inherently non-invasive, eliminating the need for biopsies or contrast agents, thereby improving patient comfort and simplifying clinical workflows. Its compact size also enables cost-effective fabrication, scalability, and seamless integration with portable diagnostic platforms. The key advantages and technical highlights of the proposed sensor are summarized in Table 3.

6. NON-INVASIVE DIAGNOSTIC CAPABILITY AND BIOCOMPATIBILITY ASSESSMENT

The non-invasive diagnostic capability and biocompatibility assessment of biosensors operating in the terahertz (THz) range

(70 THz to 3 PHz) highlight their potential in biomedical applications. These sensors leverage the unique properties of THz radiation, enabling precise detection of biological materials without the need for invasive procedures. The following sections elaborate on key aspects of this technology. Non-invasive diagnostic capability refers to three categories: (a) penetration and resolution: THz waves can penetrate dielectric materials, providing high spatial resolution for imaging and diagnostics; (b) label-free detection: the ability to analyze biological samples without markers or staining allows for real-time monitoring of molecular interactions, crucial for early disease detection; and (c) applications in cancer detection: THz sensors can identify cancerous tissues by analyzing the unique spectral signatures of biological molecules, offering a significant advantage over traditional imaging techniques. Biocompatibility assessment has similar parts including (a) non-ionizing nature: THz radiation is non-ionizing, reducing the risk of cellular damage, which is critical for patient safety; (b) material compatibility: the development of biosensors using biocompatible materials ensures that they can be safely used in vivo, minimizing adverse reactions; and (c) sensitivity and specificity: advanced sensing structures, such as metamaterials and plasmonic devices, enhance the sensitivity and specificity of biosensors, making them suitable for detecting trace biomolecules. While the advantages of THz biosensors are significant, challenges remain in enhancing their sensitivity for detecting low-concentration analytes. Continued research is essential to optimize these technologies for widespread clinical use.

7. EXPERIMENTAL CONSTRAINTS AND PROSPECTIVE VALIDATION APPROACHES

The development of nano-engineered biosensors operating in the terahertz (THz) to petahertz (PHz) frequency range presents both tremendous potential and technical challenges. Although the proposed nickel-based metamaterial absorber has not yet undergone fabrication, its theoretical design demonstrates compelling feasibility for non-invasive biomedical diagnostics. This section outlines the experimental limitations associated with high-frequency device realization, as well as future strategies for physical validation and clinical translation.

Table 3. Distinctive Features of the Proposed Nanometamaterial Sensor Design

Feature	Specification	Novelty
Size	Ultra Compact	Relatively smaller in size compared to its peers, making it suitable for integration with other portable diagnostic devices
Design	Simple	High-performance outcomes were attained using a simple design, effectively bypassing the difficulties associated with more complex structures
Fabrication feasibility	Feasible to fabricate at nanoscale level	The device can be perfectly fabricated with existing technology with cost-effective manner, thereby overcoming fabrication difficulties
Angular stability	High stability in the range 0° – 90°	Demonstrates remarkably stable performance under different incident angles
Double-negative characteristics	Accomplished in the NIR range (70–400 THz)	Demonstrates negative permittivity and negative permeability without requiring sophisticated geometries
Absorption efficiency	99%	Brilliant absorption efficiency over the entire frequency range
Operating frequency range	70 THz–3 PHz	Accomplishes a relatively broader bandwidth compared to the existing similar sensors
Nature of diagnosis	Non-invasive and label-free detection	Enables early cancer detection with non-invasive procedures and without any additional labeling agents, lowering patient's pain and discomfort
Target analyte	Cancer exosomes	Focuses on detection of circulating cancer exosomes

A. Nanoscale Fabrication at Ultra-High Frequencies

Functionality across the broad spectral range of 70 THz to 3 PHz necessitates the definition of nanostructures with sub-wavelength precision. Realizing features, such as split-ring resonators (SRRs) and complementary geometries, with consistent accuracy remains a fabrication challenge. Techniques like electron-beam lithography (EBL), focused ion beam (FIB) milling, and nanoimprint lithography (NIL) are well-suited for producing such high-resolution features, but they require access to cleanroom environments and precision process control to ensure fidelity to the simulated design.

B. Terahertz-to-Petahertz Spectral Characterization

Empirical validation of the device's absorption and sensing capabilities in the THz to PHz domain demands sophisticated spectral characterization systems, including terahertz time-domain spectroscopy (THz-TDS) and near-infrared to ultraviolet optical setups. These systems are highly sensitive to environmental variables, such as humidity and temperature, which can affect measurement consistency—especially when assessing biosensor performance in the presence of biological fluids. Controlled environmental chambers and specialized optical setups are necessary to replicate the conditions assumed in simulation environments.

C. Manufacturability and Material Compatibility

The choice of nickel as the resonator and ground plane material is both deliberate and appropriate, as it supports scalable deposition methods such as sputtering, e-beam evaporation, and atomic layer deposition. Nickel offers a favorable balance between electrical performance, structural stability, and cost-effectiveness. Its compatibility with high-throughput patterning methods, including roll-to-roll nanoimprint lithography, strengthens the case for translating the sensor architecture from concept to physical prototype.

D. Strategic Design for Clinical Integration

The sensor's compact and symmetric structure enhances its robustness and facilitates its integration into portable diagnostic systems. This structural simplicity, combined with its polarization-insensitive and broadband behavior, makes the design especially relevant for biomedical applications requiring high sensitivity and spectral selectivity across a wide frequency range.

E. Biological Testing Through Multidisciplinary Collaboration

Future validation efforts will focus on establishing collaborative studies with research institutions and clinical laboratories that specialize in oncology and biosensing. These partnerships will enable testing of the sensor with exosomal and other biofluid-derived biomarkers, under clinically relevant conditions. Validation protocols will include sensitivity analysis, specificity profiling, and performance benchmarking across various cancer indicators, establishing the biosensor's practical utility.

F. Data Interpretation and Spectral Feature Analysis

To enhance diagnostic reliability, advanced data processing techniques, such as machine learning-based classification and spectral feature extraction, may be integrated into future experimental workflows. This approach will support the interpretation of high-dimensional absorption data and improve the sensor's ability to differentiate between healthy and pathological biomarkers.

8. CONCLUSION

In this work, we have introduced a novel ultra-wideband nanobiosensor based on a double-negative (DNG) metamaterial perfect absorber (MPA), designed for early cancer detection via the identification and differentiation of circulating exosomes. Operating effectively across a broad spectral range of

70 THz to 3 PHz, with a particular focus on the near-infrared (NIR) regime (70–400 THz), the sensor exhibits near-unity absorption, robust angular and polarization insensitivity, and high field confinement, critical features for accurate and reliable biosensing.

The tri-layer Ni–SiO₂–Ni structure, optimized using full-wave electromagnetic simulations, enables simultaneous negative permittivity and permeability in the NIR band, resulting in enhanced interaction with biomolecular targets. The DNG characteristics support strong electric and magnetic resonance modes, facilitating label-free, high-sensitivity detection of exosomal biomarkers. Notably, the biosensor effectively differentiates cancer-derived exosomes from normal ones by exploiting subtle shifts in reflection coefficients and field distribution patterns.

The ultra-compact architecture, spectral selectivity, and polarization- and angle-robust performance position this sensor as a promising candidate for next-generation, non-invasive diagnostic platforms. Beyond oncological applications, the proposed design has the potential to extend to environmental sensing, photonic filtering, and energy harvesting systems.

Future work will focus on experimental validation, integration with microfluidic systems for real-time analysis, and clinical evaluation to establish its translational potential in early disease diagnostics and personalized medicine.

Funding. Taighde Éireann—Research Ireland (13/RC/2094_2); European Union's Marie Skłodowska-Curie Actions (101126578); University of Galway; University of Doha for Science and Technology (KK-2024-005); Icelandic Research Fund (2410297); Narodowe Centrum Nauki (2022/47/B/ST7/00072); Irish Research eLibrary.

Acknowledgment. Co-funded by the European Union. Views and opinions expressed are however those of the author(s) only and do not necessarily reflect those of the European Union or the European Research Executive Agency. Neither the European Union nor the granting authority can be held responsible for them. Besides that, this publication has emanated from research jointly funded by Taighde Éireann—Research Ireland, the European Union's Marie Skłodowska-Curie Actions and was supported in part by University of Galway. The authors gratefully acknowledge the financial support of the University of Doha for Science and Technology. Additionally, part of this research has been supported by the Icelandic Research Fund and the National Science Centre of Poland. Use of human participants: there were no humans involved in the study. Open access funding provided by Irish Research eLibrary.

Disclosures. The authors declare no competing interests.

Data availability. The datasets used and/or analyzed during the current study will be available from the corresponding author on reasonable request.

REFERENCES

1. M. M. K. Shuvo, M. I. Hossain, S. Mahmud, *et al.*, "Polarization and angular insensitive bendable metamaterial absorber for UV to NIR range," *Sci. Rep.* **12**, 4857 (2022).
2. R. Lai, P. Shi, Z. Yi, *et al.*, "Triple-band surface plasmon resonance metamaterial absorber based on open-ended prohibited sign type monolayer graphene," *Micromachines* **14**, 953 (2023).
3. G. V. Viktor, "The electrodynamics of substances with simultaneously negative values of ϵ and μ ," *Sov. Phys. Usp.* **10**, 509–514 (1968).
4. V. Veselago, L. Braginsky, V. Shklover, *et al.*, "Negative refractive index materials," *J. Comput. Theor. Nanosci.* **3**, 189–218 (2006).
5. D. R. Smith, J. B. Pendry, and M. C. Wiltshire, "Metamaterials and negative refractive index," *Science* **305**, 788–792 (2004).
6. W. Han, Y. Zuo, W. Zhu, *et al.*, "Selectable narrow-band anisotropic perfect absorbers based on α -MoO₃ metamaterials for refractive index sensing," *IEEE Sens. J.* **25**, 13149–13159 (2025).
7. S. Ahmed, T. Alam, P. Kirawanich, *et al.*, "Highly sensitive circle enclosed D-pad resonator-based narrowband metamaterial absorber for biosensing applications," *IEEE Sens. J.* **25**, 32536–32545 (2025).
8. M. N. Hamza, M. T. Islam, S. Lavadiya, *et al.*, "Design and validation of ultra-compact metamaterial-based biosensor for non-invasive cervical cancer diagnosis in terahertz regime," *PLOS One* **20**, e0311431 (2025).
9. S. Yin, H. Zhong, W. Huang, *et al.*, "Deep learning enabled design of terahertz high-Q metamaterials," *Opt. Laser Technol.* **181**, 111684 (2025).
10. M. N. Hamza, M. T. Islam, S. Lavadiya, *et al.*, "Ultra-compact quintuple-band terahertz metamaterial biosensor for enhanced blood cancer diagnostics," *PLOS One* **20**, e0313874 (2025).
11. W. Wang, Q. Wu, H. Li, *et al.*, "Numerical research on terahertz hyperbolic metamaterials composed of interlaced graphene-dielectric multilayers and a microcavity," *Opt. Laser Technol.* **181**, 111793 (2025).
12. M. N. Hamza, M. T. Islam, S. Lavadiya, *et al.*, "Development of a high-sensitivity triple-band nano-biosensor utilizing petahertz metamaterials for optimal absorption in early-stage leukemia detection," *IEEE Sens. J.* **25**, 13955–13973 (2025).
13. M. K. Uddin, M. T. Islam, T. Alam, *et al.*, "Polarization insensitive U-coupled splits ring resonator-based hexa-band metamaterial absorber for concentration of solid material sensing applications," *Opt. Laser Technol.* **181**, 111975 (2025).
14. J. Li, H. Chen, S. L. Yap, *et al.*, "A temperature-insensitive graphene-water-based ultra-wideband terahertz metamaterials absorber designed using deep neural networks," *Opt. Laser Technol.* **185**, 112591 (2025).
15. M. N. Hamza, M. Alibakhshikenari, B. S. Virdee, *et al.*, "Precision multi-band terahertz metamaterial biosensor with targeted spectral selectivity for early detection of MCF-7 breast cancer cells," *IEEE Sens. J.* **25**, 14970–14987 (2025).
16. M. A. Khalil, W. H. Yong, M. S. Islam, *et al.*, "A compact tri-octagonal negative index metamaterial sensor for liquid adulteration detection," *Opt. Laser Technol.* **184**, 112499 (2025).
17. H. Jiang, B. Wang, and Z. Liu, "New dual-peak High-performance structure utilizing terahertz metamaterial metasurface for concentration detection of H₂ and CH₄ gases," *Opt. Laser Technol.* **186**, 112728 (2025).
18. M. N. Hamza, M. T. Islam, S. Koziel, *et al.*, "Design of a high-sensitivity MTM-based multi-band micro-biosensor for early-stage non-melanoma skin cancer diagnosis in the terahertz region," *Opt. Laser Technol.* **192**, 114015 (2025).
19. H. Hu, H. Zhang, H. Jiang, *et al.*, "Tunable multifunctional terahertz metamaterial device based on metal-dielectric-vanadium dioxide," *Opt. Laser Technol.* **181**, 111629 (2025).
20. M. N. Hamza, M. T. Islam, S. Lavadiya, *et al.*, "Development of a terahertz metamaterial micro-biosensor for ultrasensitive multi-spectral detection of early-stage cervical cancer," *IEEE Sens. J.* **24**, 32065–32079 (2024).
21. H. Sun, L. Yang, X. Cao, *et al.*, "Terahertz perfect metasurface absorber based on groove-ring-shaped Ti₃C₂T_x MXene for refractive index sensing application," *IEEE Sens. J.* **25**, 30845–30853 (2025).
22. M. N. Hamza, M. T. Islam, and S. Koziel, "Advanced sensor for non-invasive breast cancer and brain cancer diagnosis using antenna array with metamaterial-based AMC," *Eng. Sci. Technol. Int. J.* **56**, 101779 (2024).
23. X. Zhang, Z. Wang, and Y. Gong, "Progress in multifunctional tunable terahertz metasurface waveplates," *J. Electron. Mater.* **54**, 9429–9450 (2025).
24. W. Wang, G. Li, G. Yang, *et al.*, "Enhanced multifunctionality of carbon black-modified melamine sponge: flame retardancy, electromagnetic wave absorption, and sensing capabilities," *J. Electron. Mater.* **54**, 2111–2121 (2025).
25. M. N. Hamza and M. T. Islam, "Designing an extremely tiny dual-band biosensor based on MTMs in the terahertz region as a perfect

- absorber for non-melanoma skin cancer diagnostics," *IEEE Access* **11**, 136770 (2023).
26. Y. Tong, X. Qiu, B. Lou, *et al.*, "Design and analysis of terahertz wave all-dielectric grating magnetic reflector," *J. Electron. Mater.* **54**, 3206–3216 (2025).
27. S. Sharma, A. Kumar, and T. S. Saini, "Design and simulation of a terahertz sensor for blood components detection using photonic crystal fiber," *J. Electron. Mater.* **54**, 10936–10948 (2025).
28. Y. Liu, S. Zhu, J. Geng, *et al.*, "Temperature and refractive index THz sensor based on all-dielectric InSb metasurfaces," *J. Electron. Mater.* **54**, 9782–9793 (2025).
29. B. Li, K. Ouyang, F. Li, *et al.*, "Ultra-broadband and wide-angle metamaterial absorber based on vertical three-square patches structure gallium nitride for terahertz wave," *J. Electron. Mater.* **54**, 9346–9356 (2025).
30. M. N. Hamza, M. T. Islam, S. Koziel, *et al.*, "Designing a high-sensitivity microscale triple-band biosensor based on terahertz MTMs to provide a perfect absorber for non-melanoma skin cancer diagnostic," *IEEE Photonics J.* **16**, 5900113 (2024).
31. O. Elalouy, S. Das, M. El Ghzaoui, *et al.*, "An ultra-thin polarization-sensitive quad-band metamaterial absorber (QMMA) with Ten absorption peaks for diversified advanced millimeter-wave wireless applications," *J. Electron. Mater.* **54**, 10733–10752 (2025).
32. Y. Zheng, Y. Chen, and Y. Xu, "Toroidal dipole all-dielectric metasurfaces with high sensitivity, high figure of merit, and robustness for refractive index sensing," *J. Electron. Mater.* **53**, 674–682 (2024).
33. M. N. Hamza, M. Alibakhshikenari, B. Virdee, *et al.*, "Terahertz dual-band metamaterial biosensor for cervical-cancer diagnostics," *IEEE Photonics J.* **16**, 6803011 (2024).
34. A. Teber, "A dual-band terahertz metamaterial absorber using an all-metal aluminum hexagonal metasurface structure for sensing of cancerous cells," *J. Electron. Mater.* **53**, 2686–2701 (2024).
35. M. N. Hamza, S. Koziel, and A. Pietrenko-Dabrowska, "Design and experimental validation of a metamaterial-based sensor for microwave imaging in breast, lung, and brain cancer detection," *Sci. Rep.* **14**, 16177 (2024).
36. M. N. R. Naim, J. T. Upoma, A. I. Ferdous, *et al.*, "Terahertz spectrum-based refractive index sensor for brain lesion detection using photonic crystal fibers," *Plos One* **20**, e0320355 (2025).
37. A. Miah, S. Al Zafir, M. Hasnain, *et al.*, "Triple-band highly sensitive terahertz metamaterial absorber for biomedical sensing applications," *Plos One* **20**, e0328077 (2025).
38. H.-N. Lee, Y. Park, J.-T. Park, *et al.*, "Signal preprocessing for foreign body detection using terahertz real-time non-destructive imaging system," *Plos One* **20**, e0319978 (2025).
39. M. N. Hamza, M. T. Islam, S. Lavadiya, *et al.*, "Designing a high-sensitivity dual-band nano-biosensor based on petahertz MTMs to provide a perfect absorber for early-stage non-melanoma skin cancer diagnostic," *IEEE Sens. J.* **24**, 18418–18427 (2024).
40. A. M. T. Hoque, A. Islam, F. Haider, *et al.*, "Point-of-care testing of hyponatremia and hypernatremia levels: an optoplasmonic biosensing approach," *PLoS One* **20**, e0319559 (2025).
41. A. I. Ferdous, M. S. Hosen, K. Khandakar, *et al.*, "Pioneering terahertz blood analysis: hollow-core PCF with optimized sensitivity and low loss," *PLoS One* **20**, e0319860 (2025).
42. M. M. Bani, M. Mynuddin, K. S. Noor, *et al.*, "Towards point-of-care HIV testing: terahertz PCF sensor integration and miniaturization," *PLoS One* **20**, e0327357 (2025).
43. M. N. Hamza and M. T. Islam, "Design of MTM-based multi-band micro-biosensor in terahertz region as perfect absorber for early-stage leukemia diagnosis with sensitivity 18626373 THz/RIU," *IEEE Sens. J.* **24**, 16055–16069 (2024).
44. M. M. Kamal, I. Khan, M. Al-Khasawneh, *et al.*, "Hybrid optimization-based deep learning for energy efficiency resource allocation in MIMO-enabled wireless networks," *Sci. Rep.* **15**, 31642 (2025).
45. M. M. Kamal, S. Yang, S. H. Kiani, *et al.*, "A novel hook-shaped antenna operating at 28 GHz for future 5G mmwave applications," *Electronics* **10**, 673 (2021).
46. I. Khan, C. Song, H. Ullah, *et al.*, "Investigation of coplanar waveguide fed SWB antenna with controllable stop band characteristics," *Sci. Rep.* **15**, 14051 (2025).
47. I. Khan, C. Song, H. Ullah, *et al.*, "A novel multiband low mutual coupling quad-element MIMO antenna for advanced communication systems," *IEEE Access* **13**, 65198–65215 (2025).
48. M. Y. Azab, M. F. O. Hameed, A. M. Nasr, *et al.*, "Highly sensitive metamaterial biosensor for cancer early detection," *IEEE Sens. J.* **21**, 7748–7755 (2021).
49. S. K. Patel, J. Surve, and J. Parmar, "Detection of cancer with graphene metasurface-based highly efficient sensors," *Diam. Relat. Mater.* **129**, 109367 (2022).
50. B. Amini and Z. Atlasbaf, "Design and analysis of high-sensitivity tunable graphene sensors for cancer detection," *Opt. Quantum Electron.* **55**, 446 (2023).
51. P. Upender and A. Kumar, "THz dielectric metamaterial sensor with high Q for biosensing applications," *IEEE Sens. J.* **23**, 5737–5744 (2023).
52. S. Banerjee, U. Nath, P. Dutta, *et al.*, "A theoretical terahertz metamaterial absorber structure with a high quality factor using two circular ring resonators for biomedical sensing," *Inventions* **6**, 78 (2021).
53. Z. Geng, X. Zhang, Z. Fan, *et al.*, "A route to terahertz metamaterial biosensor integrated with microfluidics for liver cancer biomarker testing in early stage," *Sci. Rep.* **7**, 16378 (2017).
54. H. E. Nejad, A. Mir, and A. Farmani, "Supersensitive and tunable nano-biosensor for cancer detection," *IEEE Sens. J.* **19**, 4874–4881 (2019).
55. D. Li, F. Hu, H. Zhang, *et al.*, "Identification of early-stage cervical cancer tissue using metamaterial terahertz biosensor with two resonant absorption frequencies," *IEEE J. Sel. Top. Quantum Electron.* **27**, 8600107 (2021).
56. S. Banerjee, P. Dutta, A. V. Jha, *et al.*, "A biomedical sensor for detection of cancer cells based on terahertz metamaterial absorber," *IEEE Sens. Lett.* **6**, 6002004 (2022).
57. A. Chaudhuri, B. Rai, and P. Pal, "Design of a dual-band metasurface cross-polarization converter for cancer detection in the terahertz band," *IEEE Sens. J.* **24**, 7292–7298 (2023).
58. J. Chen, F. Hu, X. Ma, *et al.*, "Deep neural network assisted terahertz metasurface sensors for the detection of lung cancer biomarkers," *IEEE Sens. J.* **24**, 15698–15705 (2024).
59. A. Hlali, A. Oueslati, and H. Zairi, "Numerical simulation of tunable terahertz graphene-based sensor for breast tumor detection," *IEEE Sens. J.* **21**, 9844–9851 (2021).
60. X. Hou, F. Hu, L. Zhang, *et al.*, "Cancer biomarkers ultrasensitive detection based on terahertz frequency-comb-like," *IEEE Sens. J.* **23**, 10413–10419 (2023).
61. A. Veeraselvam, G. N. A. Mohammed, K. Savarimuthu, *et al.*, "An ultra-thin multiband refractive index-based carcinoma sensor using THz radiation," *IEEE Sens. J.* **22**, 2045–2052 (2021).
62. D. Xie, D. Li, F. Hu, *et al.*, "Terahertz metamaterial biosensor with double resonant frequencies for specific detection of early-stage hepatocellular carcinoma," *IEEE Sens. J.* **23**, 1124–1131 (2022).
63. F. Wahaia, G. Valusis, L. M. Bernardo, *et al.*, "Detection of colon cancer by terahertz techniques," *J. Mol. Struct.* **1006**, 77–82 (2011).
64. M. Rezeg, A. Hlali, and H. Zairi, "THz biomedical sensing for early cancer detection: metamaterial graphene biosensors with rotated split-ring resonators," *IEEE Photonics J.* **16**, 2100110 (2024).
65. L. Yu, L. Hao, T. Meiqiong, *et al.*, "The medical application of terahertz technology in non-invasive detection of cells and tissues: opportunities and challenges," *RSC Adv.* **9**, 9354–9363 (2019).
66. G. Valušis, A. Lisauskas, H. Yuan, *et al.*, "Roadmap of terahertz imaging 2021," *Sensors* **21**, 4092 (2021).
67. W. Zhang, J. Lin, Z. Yuan, *et al.*, "Terahertz metamaterials for biosensing applications: a review," *Biosensors* **14**, 3 (2023).
68. C. Tan, S. Wang, S. Li, *et al.*, "Cancer diagnosis using terahertz-graphene-metasurface-based biosensor with dual-resonance response," *Nanomaterials* **12**, 3889 (2022).
69. Q. Liu, T. Ning, L. Pei, *et al.*, "Q-BIC THz metasurface biosensor based on flexible polyimide for solution detection," *IEEE Sens. J.* **25**, 11008–11015 (2025).

70. L. Shen, H. Liu, X. Ke, *et al.*, "Label-free detection of biological cells using quasi-bound states in the continuum with terahertz metasurface," *IEEE Sens. J.* **25**, 10984–10991 (2025).
71. L. Chi, Y. Liu, W. Zhou, *et al.*, "Broadband infrared to terahertz detection based on pyramidal polymer-derived ceramic array absorber," *IEEE Sens. J.* **25**, 14960–14969 (2025).
72. X. Chen, L. Ye, and D. Yu, "Terahertz hybrid detection of chiral enantiomers with intrinsic low absorption enabled by metasurface," *IEEE Sens. J.* **25**, 6301–6308 (2025).
73. N. I. Landy, S. Sajuyigbe, J. J. Mock, *et al.*, "Perfect metamaterial absorber," *Phys. Rev. Lett.* **100**, 207402 (2008).
74. S. Park, J. T. Hong, S. J. Choi, *et al.*, "Detection of microorganisms using terahertz metamaterials," *Sci. Rep.* **4**, 4988 (2014).
75. S. Park, S. Cha, G. Shin, *et al.*, "Sensing viruses using terahertz nano-gap metamaterials," *Biomed. Opt. Express* **8**, 3551–3558 (2017).
76. J. P. Turpin, J. A. Bossard, K. L. Morgan, *et al.*, "Reconfigurable and tunable metamaterials: a review of the theory and applications," *Int. J. Antennas Propag.* **2014**, 429837 (2014).
77. T. Cao, C.-W. Wei, R. E. Simpson, *et al.*, "Broadband polarization-independent perfect absorber using a phase-change metamaterial at visible frequencies," *Sci. Rep.* **4**, 3955 (2014).
78. N. Liu, H. Guo, L. Fu, *et al.*, "Three-dimensional photonic metamaterials at optical frequencies," *Nat. Mater.* **7**, 31–37 (2008).
79. S. Mahmud, S. S. Islam, K. Mat, *et al.*, "Design and parametric analysis of a wide-angle polarization-insensitive metamaterial absorber with a star shape resonator for optical wavelength applications," *Results Phys.* **18**, 103259 (2020).
80. F. Yang, R.-H. Li, S.-L. Tan, *et al.*, "Visible-mid infrared ultra-broadband and wide-angle metamaterial perfect absorber based on cermet films with nano-cone structure," *Nanophotonics* **12**, 2451–2460 (2023).
81. L. Lei, S. Li, H. Huang, *et al.*, "Ultra-broadband absorber from visible to near-infrared using plasmonic metamaterial," *Opt. Express* **26**, 5686–5693 (2018).
82. R. M. H. Bilal, M. A. Saeed, M. A. Naveed, *et al.*, "Nickel-based high-bandwidth nanostructured metamaterial absorber for visible and infrared spectrum," *Nanomaterials* **12**, 3356 (2022).
83. W. Cao, H.-D. Chen, Y.-W. Yu, *et al.*, "Changing profiles of cancer burden worldwide and in China: a secondary analysis of the global cancer statistics 2020," *Chin. Med. J.* **134**, 783–791 (2021).
84. M. Entezari, M. Ghanbarirad, A. Taheriazam, *et al.*, "Long non-coding RNAs and exosomal lncRNAs: potential functions in lung cancer progression, drug resistance and tumor microenvironment remodeling," *Biomed. Pharmacother.* **150**, 112963 (2022).
85. M. D. A. Paskeh, M. Entezari, S. Mirzaei, *et al.*, "Emerging role of exosomes in cancer progression and tumor microenvironment remodeling," *J. Hematol. Oncol.* **15**, 83 (2022).
86. N. A. Hanjani, N. Esmaelizad, S. Zanganeh, *et al.*, "Emerging role of exosomes as biomarkers in cancer treatment and diagnosis," *Crit. Rev. Oncol./Hematol.* **169**, 103565 (2022).
87. Q. Maqsood, A. Sumrin, Y. Saleem, *et al.*, "Exosomes in cancer: diagnostic and therapeutic applications," *Clin. Med. Insights Oncol.* **18**, 11795549231215966 (2024).
88. Y. Van Der Pol and F. Mouliere, "Toward the early detection of cancer by decoding the epigenetic and environmental fingerprints of cell-free DNA," *Cancer Cell* **36**, 350–368 (2019).
89. F. Arshad, F. Nabi, S. Iqbal, *et al.*, "Applications of graphene-based electrochemical and optical biosensors in early detection of cancer biomarkers," *Colloids Surf. B* **212**, 112356 (2022).
90. X. Chen, J. Gole, A. Gore, *et al.*, "Non-invasive early detection of cancer four years before conventional diagnosis using a blood test," *Nat. Commun.* **11**, 3475 (2020).
91. N. Pashayan and P. D. Pharoah, "The challenge of early detection in cancer," *Science* **368**, 589–590 (2020).
92. S. V. Gaponenko, *Introduction to Nanophotonics* (Cambridge University, 2010).
93. Q. Chen, X. Hu, L. Wen, *et al.*, "Nanophotonic image sensors," *Small* **12**, 4922–4935 (2016).
94. K. W. Mauser, S. Kim, S. Mitrovic, *et al.*, "Resonant thermoelectric nanophotonics," *Nat. Nanotechnol.* **12**, 770–775 (2017).
95. C. Simovski and S. Tretyakov, *An Introduction to Metamaterials and Nanophotonics* (Cambridge University, 2020).
96. A. Kuzin, V. Chernyshev, V. Kovalyuk, *et al.*, "Real-time surface functionalization of a nanophotonic sensor for liquid biopsy," *Appl. Phys. Lett.* **123**, 193702 (2023).
97. I. H. Chowdhury, M. M. R. Mazumder, S. S. Islam, *et al.*, "Ultrawideband nanostructured metamaterial absorber with an octagon-packed star-shaped resonator for UV to NIR spectrum wavelength application," *Ain Shams Eng. J.* **15**, 102653 (2024).
98. A. Musa, T. Alam, M. T. Islam, *et al.*, "Broadband plasmonic metamaterial optical absorber for the visible to near-infrared region," *Nanomaterials* **13**, 626 (2023).
99. S. Jiao, Y. Li, H. Yang, *et al.*, "Numerical study of ultra-broadband wide-angle absorber," *Results Phys.* **24**, 104146 (2021).
100. R. M. H. Bilal, S. Zakir, M. A. Naveed, *et al.*, "Nanoengineered nickel-based ultrathin metamaterial absorber for the visible and short-infrared spectrum," *Opt. Mater. Express* **13**, 28–40 (2023).
101. D. Wu, L. Lei, M. Xie, *et al.*, "High-performance metamaterial light absorption from visible to near-infrared assisted by anti-reflection coating," *Photonics* **10**, 998 (2023).
102. M. S. Raean, A. Nella, and R. Maheswar, "A fourfold star petal-shaped polarization-insensitive broadband plasmonic metamaterial absorber," *Plasmonics* **18**, 1059–1074 (2023).